

This is the accepted manuscript made available via CHORUS. The article has been published as:

Tunable inverse topological heterostructure utilizing
 $(\text{Bi}_{1-x}\text{In}_x)_2\text{Se}_3$ and multichannel weak-
antilocalization effect

Matthew J. Brahlek, Nikesh Koirala, Jianpeng Liu, Tahir I. Yusufaly, Maryam Salehi, Myung-Geun Han, Yimei Zhu, David Vanderbilt, and Seongshik Oh

Phys. Rev. B **93**, 125416 — Published 10 March 2016

DOI: [10.1103/PhysRevB.93.125416](https://doi.org/10.1103/PhysRevB.93.125416)

Tunable inverse topological heterostructure utilizing $(\text{Bi}_{1-x}\text{In}_x)_2\text{Se}_3$ and multi-channel weak-antilocalization effect

Matthew J. Brahlek^{1†#}, Nikesh Koirala^{1†}, Jianpeng Liu¹, Tahir I. Yusufaly¹, Maryam Salehi², Myung-Geun Han³, Yimei Zhu³, David Vanderbilt¹, and Seongshik Oh^{1,*}

¹Department of Physics & Astronomy, Rutgers, The State University of New Jersey, Piscataway, New Jersey 08854, U.S.A.

²Department of Materials Science and Engineering, Rutgers, The State University of New Jersey, Piscataway, New Jersey 08854, U.S.A.

³Condensed Matter Physics & Materials Science, Brookhaven National Lab, Upton, NY 11973, U.S.A.

[†]These authors contributed equally to this work

[#]Present address: Department of Materials Science and Engineering, Pennsylvania State University, University Park, Pennsylvania 16802, U.S.A.

*ohsean@physics.rutgers.edu

Abstract: In typical topological insulator (TI) systems the TI is bordered by a non-TI insulator, and the surrounding conventional insulators, including vacuum, are not generally treated as part of the TI system. Here, we implement the first material system where the roles are reversed, and the TSS form around the non-TI (instead of the TI) layers. This is realized by growing a layer of the tunable non-TI $(\text{Bi}_{1-x}\text{In}_x)_2\text{Se}_3$ in between two layers of the TI Bi_2Se_3 using the atomically-precise molecular beam epitaxy technique. On this tunable inverse topological platform, we systematically vary the thickness and the composition of the $(\text{Bi}_{1-x}\text{In}_x)_2\text{Se}_3$ layer and show that this tunes the coupling between the TI layers from strongly-coupled metallic to weakly-coupled, and finally to a fully-decoupled insulating regime. This system can be used to probe the fundamental nature of coupling in TI materials and provides a tunable insulating layer for TI devices.

The topological classification scheme is rooted in the ability to distil the global properties of an object into a single number known as a topological invariant. This notion of topology can be extended from the archetypal example of geometric topology, where shapes are classified based solely on the number of holes, to electronic materials, where the main physical implication occurs on the boundary between materials that belong to different topological classes. In the 3-dimensional (3D) class of topological insulators (TIs) unusual topological surface states (TSS) form on the 2-dimensional (2D) boundary with non-TIs. These surface states have metallic, gapless energy bands, which disperse linearly with momentum like photons, and the spins of the surface electrons are locked perpendicular to the direction of their momentum (see refs. [1,2]). TSS have been experimentally confirmed by various surface sensitive probes such as angle-resolved photo emission spectroscopy [3–5], scanning tunneling microscopy [6], and more recently, transport measurements [7–16].

The TSS are an entirely interfacial phenomenon, which form across the interface between a TI and a trivial insulator. As shown in Fig. 1(a), experiments to probe the nature of the TSS thus far have viewed them as forming at the interface between a single-slab TI and a trivial insulator such as vacuum. However, as depicted in Fig. 1(b), equivalent TSS will form at the interfaces when the role of the trivial insulator and the TI are reversed. Such an inverted structure is physically attainable, and provides new opportunities that cannot be accessed in existing TI materials. Using the atomic precision of the molecular beam epitaxy (MBE) technique, we report the first implementation of such a system by inserting a layer of a tunable non-TI $(\text{Bi}_{1-x}\text{In}_x)_2\text{Se}_3$ (bandgap ~ 1.3 eV at $x = 100\%$ [17–20]) between two layers of the TI Bi_2Se_3 [21,22], as shown in Fig. 1(c). This tunable inverse topological (TIT) system allows us to investigate how the conducting channels interact through the bulk $(\text{Bi}_{1-x}\text{In}_x)_2\text{Se}_3$ layer in a regime far beyond what is accessible in any existing TI materials: from a strong insulator with a bandgap of ~ 1.3 eV, which is far greater than those (~ 0.3 eV) of existing TIs, all the way down to a zero-gap semimetal. It is also important to note that $(\text{Bi}_{1-x}\text{In}_x)_2\text{Se}_3$ is unique as a component for TI heterostructures in that it is the only non-TI material that shares the same crystal structure with a TI: this is critical for the formation of atomically smooth interfaces as seen in Fig. 1(c).

By varying the thickness of the non-TI barrier layer from the ultra-thin (1 quintuple layer, 1 QL \approx 1 nm) to the thick regime (> 100 QL), we find that the Bi_2Se_3 layers become electrically isolated at an In_2Se_3 thickness of ~ 3 QL, as shown by transport measurements, and first-principles calculations indicate that this coincides with the emergence of the TSS. Further, by decreasing x in the $(\text{Bi}_{1-x}\text{In}_x)_2\text{Se}_3$ barrier layer from $x = 100\%$ to 30% , the conduction band offset (potential barrier height) is lowered, and the coupling strength gradually increases for a fixed barrier layer thickness. For a fixed composition x , the Bi_2Se_3 layers undergo a coupled-to-decoupled transition as the thickness grows beyond a critical value. However, when x is reduced below $\sim 30\%$, the barrier layer becomes metallic and the system remains fully coupled over the entire thickness range.

The weak anti-localization (WAL) effect is a common feature of the magneto-resistance in strongly spin-orbit-coupled 2D systems such as TI thin films (see Supplemental Materials for measurement geometry, and note that both layers of Bi_2Se_3 are electrically contacted using In contacts) [10,12,13,15,16,23–28]. As shown in Fig. 2(a), the WAL effect is typically seen as a sharp cusp at small field in resistance vs magnetic field, which is fit by the Hikami-Larkin-Nagaoka (HLN) formula $\Delta G(B) = -\tilde{A}e^2/(2\pi h)(\ln[\hbar/(4el_\phi^2 B)] - \Psi[1/2 + \hbar/(4el_\phi^2 B)])$, where h is Planck's constant, e is the electron charge, Ψ is the digamma function, and the two fitting parameters are \tilde{A} , a constant, and l_ϕ , the de-phasing length [29]. In general l_ϕ is limited by the inelastic scattering length, which depends strongly on microscopic details such as disorder and phonons (see Fig. S6 in Supplemental Materials). In contrast, \tilde{A} has been found to be much more robust. In single slab Bi_2Se_3 layers it has been found that $\tilde{A} \approx 1$ due to the conducting bulk state, which mediates electrical coupling between the surface transport channels in the film. However, recent studies show that \tilde{A} can increase to 2 if the top and bottom surface channels in TI films are electrically isolated from each other [12,13,15,16,23]. These observations show that \tilde{A} represents the number of decoupled 2D conducting channels in strongly spin-orbit-coupled systems, thus providing a means to probe the coupling strength between adjacent 2D channels. Therefore, as we show below, the TIT heterostructure allows us to take two adjacent Bi_2Se_3 layers, each with $\tilde{A} \approx 1$, and

determine their electric coupling by tracking \tilde{A} . Using this, we fully map out the dependence of the interlayer coupling on both composition and thickness of the $(\text{Bi}_{1-x}\text{In}_x)_2\text{Se}_3$ barrier layer.

By introducing an In_2Se_3 layer in the center of a 60-QL Bi_2Se_3 slab (*i.e.* $\text{Bi}_2\text{Se}_3\text{-In}_2\text{Se}_3\text{-Bi}_2\text{Se}_3$ with thicknesses 30- t -30 QL) induces an $\tilde{A} = 1 \rightarrow 2$ transition with increasing In_2Se_3 thickness t , as shown in Fig. 2(b), which implies that beyond a critical thickness of the In_2Se_3 layer, the top and bottom TI layers become decoupled. Due to the large bandgap of In_2Se_3 , ~ 1.3 eV, compared with ~ 0.3 eV for Bi_2Se_3 , the top and bottom Bi_2Se_3 layers become electrically isolated for barrier thicknesses as small as ~ 3 QL, whereas a similar transition occurs only above ~ 20 QL of separation between the two surfaces in bulk insulating single-slab Bi_2Se_3 films [15,16,26] and no such transition occurs in the commonly available bulk-metallic single-slab Bi_2Se_3 films [26]. Figure 2(c) shows an extension of this experiment where another unit of $\text{Bi}_2\text{Se}_3\text{-In}_2\text{Se}_3$ has been added ($\text{Bi}_2\text{Se}_3\text{-In}_2\text{Se}_3\text{-Bi}_2\text{Se}_3\text{-In}_2\text{Se}_3\text{-Bi}_2\text{Se}_3$ with corresponding thicknesses of 30-20-30- t -30 QL); \tilde{A} responds by transitioning from $2 \rightarrow 3$ with increasing In_2Se_3 thickness, which confirms and extends the counting nature of the \tilde{A} parameter.

To understand the microscopic origin of this transition, we carried out first-principles calculations based on density-functional theory (DFT). We first performed calculations on bulk Bi_2Se_3 and In_2Se_3 , which were extended to $\text{Bi}_2\text{Se}_3\text{-In}_2\text{Se}_3$ supercells by allowing the construction of Wannierized effective Hamiltonians (see Supplemental Materials for more details). Figure 2(d) shows that the bandgap at the Γ point near the interface of $\text{Bi}_2\text{Se}_3\text{-In}_2\text{Se}_3$ closes with increasing In_2Se_3 thickness as the wavefunction overlap between the interfacial states dies out. The spatial electronic properties can be further seen by tracking the real space density of the states around the Fermi level (RDOS, see ref. [30] and Supplemental Materials), as shown in Fig. 2(e-h). This calculation shows that the RDOS increases near the $\text{Bi}_2\text{Se}_3\text{-In}_2\text{Se}_3$ interface even for a single QL of In_2Se_3 , indicating a new state has begun to emerge. By 2-3 QL of In_2Se_3 , the RDOS splits, peaking near the $\text{Bi}_2\text{Se}_3\text{-In}_2\text{Se}_3$ interfaces and diminishing near the center, which implies the formation of the gapless interfacial states and the development of an insulating bulk state in the middle of In_2Se_3 . The finite density of states in the In_2Se_3 region is due to the evanescent decay of the TSS wavefunctions into the In_2Se_3 layer, and extends around ~ 2 QL into the In_2Se_3 layer, which is better

seen for the relatively thick 8 QL In_2Se_3 in Fig. 2(h). This shows that the emergence of the interface states from the DFT calculation coincides with the WAL $\tilde{A} = 1 \rightarrow 2$ transition, both of which suggest that the two Bi_2Se_3 layers are fully isolated beyond ~ 3 QL of In_2Se_3 .

We can extend the ability to engineer and explore how the $\tilde{A} = 1 \rightarrow 2$ transition evolves by mixing Bi into the In_2Se_3 barrier layer, which controls the insulating properties of the barrier layer. It was previously shown that $(\text{Bi}_{1-x}\text{In}_x)_2\text{Se}_3$ undergoes a composition-dependent topological and metal-insulator phase transitions: it first undergoes a TI to non-TI transition near $x \approx 3 - 7\%$ [18–20], then transitions into a weakly insulating variable-range-hopping state near $x \approx 15\%$ and finally into a strong band insulator for $x > 25\%$ [18]. Therefore, by adjusting x , we can control the coupling strength between the TI layers. This process is sketched in Fig. 3 (a), and demonstrated by plots of \tilde{A} versus $(\text{Bi}_{1-x}\text{In}_x)_2\text{Se}_3$ thickness in Fig. 3 (b-d), which show that as x decreases from 40 to 30 and to 20%, the transition region is pushed to larger thickness, and Fig. 3(e-g), which show that in \tilde{A} versus composition at fixed thickness the transition occurs at smaller In composition with increasing thickness.

As shown in Fig. 2 (b-c) and Fig. 3 (b-d), the barrier thickness dependence of \tilde{A} is well fit by a smoothed step function, $\tilde{A}(t) = 2 - 1/(1 + e^{2(t-t_0)/l_0})$, which is characterized by the critical transition thickness t_0 and the transition width l_0 . We have plotted the values of the fitting parameters t_0 and l_0 in Fig. 3(h), and it can be seen that for $x \gtrsim 30\%$, both t_0 and l_0 are approximately exponential functions of x . However, the empirical exponential dependence breaks down below $x = 30\%$. For $x \gtrsim 30\%$, we fit the experimental behavior to $t_0(x) = \tau e^{-x/x_0}$ and $l_0(x) = \lambda e^{-x/x_0}$, resulting in $\tau \approx 90$ nm, $\lambda \approx 60$ nm, and both t_0 and l_0 consistently yield $x_0 \approx 25\%$, which coincides with the composition where the exponential trend breaks down. In order to see this breakdown more clearly, we generated the red dotted curve for $x = 20\%$ in Fig. 3(d) by extrapolating the exponential behavior to $x = 20\%$ (see the red stars in Fig. 3(h)); this curve clearly deviates from the experimental data for $x = 20\%$. The origin of this transition is likely due to the intrinsically high Fermi level in these materials: in an ideal TI, the Fermi level ($E_{F, \text{Ideal}}$) is naturally at the Dirac point, whereas in real materials, the Fermi level is close to but above the bottom of the bulk

conduction band ($E_{F,Real}$). Therefore, due to the natural position of the Fermi level, the barrier layer will become metallic when the conduction bands of the Bi_2Se_3 layers and the $(\text{Bi}_{1-x}\text{In}_x)_2\text{Se}_3$ barrier layer cross, which, as detailed in the Supplemental Materials, occurs near $x \approx 25\%$. This indicates that below $x \approx 25\%$, the insulating behavior of $(\text{Bi}_{1-x}\text{In}_x)_2\text{Se}_3$ fully breaks down, and gives way to a metallic regime, which coincides with the known composition where the band-insulating state dies out in homogeneous $(\text{Bi}_{1-x}\text{In}_x)_2\text{Se}_3$ films [18].

Figure 3(e-g) shows how \tilde{A} changes with x for fixed barrier thicknesses (10, 20 and 30 QL). For each thickness, \tilde{A} transitions from 1 to 2 with increasing x . If the empirical exponential dependence of t_0 and l_0 on x holds, then there should be enough information to generate a curve that fits these data points. Using $\tilde{A}(t) = 2 - \frac{1}{1+e^{2(t-t_0)/l_0}}$ $\rightarrow \tilde{A}(t, x) = 2 - \frac{1}{1+e^{2(t-t_0(x))/l_0(x)}}$, where $l_0(x) \approx 60e^{-x/25}$ and $t_0(x) \approx 90e^{-x/25}$ (the numerical values were obtained above) allows the generation of the curves for \tilde{A} vs x (for greater than $\sim 25\%$) with *no free parameters*. The solid red curves in Fig. 3(e-g) agree well with the experimental data for $x > 25\%$, and this further confirms that the empirical exponential relations for l_0 and t_0 hold for all x greater than $\sim 25\%$. Figure 3(i) summarizes the behavior of \tilde{A} as a function of thickness t and composition x . The well-defined behavior of \tilde{A} with both x and t suggests the presence of a fundamental underlying mechanism. However, the exponential dependence of the parameters on composition is not yet understood, and further studies will be needed to fully resolve this.

Much like the TSS that form around the bulk state in a TI, we have shown that in our TIT heterostructure system the coupling between the two TIs is determined solely by the properties of the middle $(\text{Bi}_{1-x}\text{In}_x)_2\text{Se}_3$ layer, which transitions from a full insulator to a semi-metal depending on its composition and thickness. Going forward, the unique properties of $(\text{Bi}_{1-x}\text{In}_x)_2\text{Se}_3$ can be utilized as a tunnel barrier and gate dielectric, which are essential components of many TI devices such as spin injection devices, topological tunnel junctions and field effect transistors. First, it is the only material that has a seamless interface with the TI Bi_2Se_3 . Second, its barrier properties are finely adjustable through the Bi/In ratio. As such, we anticipate that this study will stimulate utilization of $(\text{Bi}_{1-x}\text{In}_x)_2\text{Se}_3$ in various TI

nanostructures and devices leading to further discoveries and applications. Finally, it is worth noting that the concept of inserting a tunable barrier layer between 2D channels as a way to manipulate their electronic properties can be applied to non-TI systems as well. Comparing and testing how the electronic properties evolve as various 2D channels merge or split while maintaining the 2D nature will be an interesting subject of future studies.

Acknowledgements

This work is supported by NSF (DMR-1308142, DMR-1005838, and DMREF-1233349), and Gordon and Betty Moore Foundation's EPiQS Initiative (GBMF4418). The work at Brookhaven National Lab is supported by U.S. Department of Energy, Office of Basic Energy Science, Division of Materials Science and Engineering under Contract number DE-AC02-98CH10886. We acknowledge J. Garlow for TEM sample preparation using focused-ion beam at Center for Functional Nanomaterials, Brookhaven National Lab.

References

- [1] M. Z. Hasan and C. L. Kane, *Rev. Mod. Phys.* **82**, 3045 (2010).
- [2] X.-L. Qi and S.-C. Zhang, *Rev. Mod. Phys.* **83**, 1057 (2011).
- [3] Y. L. Chen, J. G. Analytis, J.-H. Chu, Z. K. Liu, S.-K. Mo, X. L. Qi, H. J. Zhang, D. H. Lu, X. Dai, Z. Fang, S. C. Zhang, I. R. Fisher, Z. Hussain, and Z.-X. Shen, *Science* **325**, 178 (2009).
- [4] D. Hsieh, D. Qian, L. Wray, Y. Xia, Y. S. Hor, R. J. Cava, and M. Z. Hasan, *Nature* **452**, 970 (2008).
- [5] Y. Xia, D. Qian, D. Hsieh, L. Wray, A. Pal, H. Lin, A. Bansil, D. Grauer, Y. S. Hor, R. J. Cava, and M. Z. Hasan, *Nat. Phys.* **5**, 398 (2009).
- [6] P. Roushan, J. Seo, C. V Parker, Y. S. Hor, D. Hsieh, D. Qian, A. Richardella, M. Z. Hasan, R. J. Cava, and A. Yazdani, *Nature* **460**, 1106 (2009).
- [7] J. G. Analytis, R. D. McDonald, S. C. Riggs, J.-H. Chu, G. S. Boebinger, and I. R. Fisher, *Nat. Phys.* **6**, 960 (2010).
- [8] N. P. Butch, K. Kirshenbaum, P. Syers, A. B. Sushkov, G. S. Jenkins, H. D. Drew, and J. Paglione, *Phys. Rev. B* **81**, 241301 (2010).
- [9] H. Steinberg, D. R. Gardner, Y. S. Lee, and P. Jarillo-Herrero, *Nano Lett.* **10**, 5032 (2010).
- [10] M. Liu, C.-Z. Chang, Z. Zhang, Y. Zhang, W. Ruan, K. He, L. Wang, X. Chen, J.-F. Jia, S.-C. Zhang, Q.-K. Xue, X. Ma, and Y. Wang, *Phys. Rev. B* **83**, 165440 (2011).
- [11] J. G. Checkelsky, Y. S. Hor, R. J. Cava, and N. P. Ong, *Phys. Rev. Lett.* **106**, 196801 (2011).
- [12] Y. S. Kim, M. Brahlek, N. Bansal, E. Edrey, G. A. Kapilevich, K. Iida, M. Tanimura, Y. Horibe, S. W. Cheong, and S. Oh, *Phys. Rev. B* **84**, 073109 (2011).
- [13] N. Bansal, Y. S. Kim, M. Brahlek, E. Edrey, and S. Oh, *Phys. Rev. Lett.* **109**, 116804 (2012).
- [14] D. Kim, S. Cho, N. P. Butch, P. Syers, K. Kirshenbaum, S. Adam, J. Paglione, and M. S. Fuhrer, *Nat. Phys.* **8**, 459 (2012).
- [15] D. Kim, P. Syers, N. P. Butch, J. Paglione, and M. S. Fuhrer, *Nat. Commun.* **4**, 2040 (2013).
- [16] M. Brahlek, N. Koirala, M. Salehi, N. Bansal, and S. Oh, *Phys. Rev. Lett.* **113**, 026801 (2014).
- [17] Y. Watanabe, S. Kaneko, H. Kawazoe, and M. Yamane, *Phys. Rev. B* **40**, 3133 (1989).
- [18] M. Brahlek, N. Bansal, N. Koirala, S.-Y. Xu, M. Neupane, C. Liu, M. Z. Hasan, and S. Oh, *Phys. Rev. Lett.* **109**, 186403 (2012).
- [19] L. Wu, M. Brahlek, R. Valdés Aguilar, A. V. Stier, C. M. Morris, Y. Lubashevsky, L. S. Bilbro, N. Bansal, S. Oh, and N. P. Armitage, *Nat. Phys.* **9**, 410 (2013).
- [20] J. Liu and D. Vanderbilt, *Phys. Rev. B* **88**, 224202 (2013).
- [21] Z. Y. Wang, X. Guo, H. D. Li, T. L. Wong, N. Wang, and M. H. Xie, *Appl. Phys. Lett.* **99**, 23112 (2011).
- [22] Y. Zhao, H. Liu, X. Guo, Y. Jiang, Y. Sun, H. Wang, Y. Wang, H.-D. Li, M.-H. Xie, X.-C. Xie, and J. Wang, *Nano Lett.* **14**, 5244 (2014).
- [23] H. Steinberg, J. B. Laloë, V. Fatemi, J. S. Moodera, and P. Jarillo-Herrero, *Phys. Rev. B* **84**, 233101 (2011).
- [24] J. Chen, X. Y. He, K. H. Wu, Z. Q. Ji, L. Lu, J. R. Shi, J. H. Smet, and Y. Q. Li, *Phys. Rev. B* **83**, 241304 (2011).

- [25] J. J. Cha, D. Kong, S.-S. Hong, J. G. Analytis, K. Lai, and Y. Cui, *Nano Lett.* **12**, 1107 (2012).
- [26] M. Brahlek, N. Koirala, N. Bansal, and S. Oh, *Solid State Commun.* **215**, 54 (2014).
- [27] I. Garate and L. Glazman, *Phys. Rev. B* **86**, 035422 (2012).
- [28] H.-Z. Lu and S.-Q. Shen, *Phys. Rev. B* **84**, 125138 (2011).
- [29] S. Hikami, A. I. Larkin, and N. Nagaoka, *Prog. Theor. Phys.* **63**, 707 (1980).
- [30] Q. Zhang, Z. Zhang, Z. Zhu, U. Schwingenschlögl, and Y. Cui, *ACS Nano* **6**, 2345 (2012).

Figure Captions

Figure 1. (Color online) Schematic and TEM image comparing the single-slab TI vs inverse TI heterostructure. (a-b) Topological surface states form when there is a change in topological invariant (ν) across an interface (*i.e.* $\Delta\nu = 1$). (a) Single-slab TI: a topological material (characterized by a topological invariant $\nu_{TI} = 1$) surrounded by non-topological insulator ($\nu_{nTI} = 0$), which forms a metallic topological surface state at the interface (indicated by the arrows). (b) Inverse TI geometry formed by inverting the role of non-TI and the topological material, and a nominally identical surface state forms at this interface. (c) High-resolution high-angle annular dark-field scanning transmission electron microscopy image showing the physical realization of the inverse TI geometry (b) in a $\text{Bi}_2\text{Se}_3\text{-In}_2\text{Se}_3\text{-Bi}_2\text{Se}_3$ heterostructure.

Figure 2. (Color online) Weak anti-localization and first principles calculations for $\text{Bi}_2\text{Se}_3\text{-In}_2\text{Se}_3\text{-Bi}_2\text{Se}_3$ films. (a) The measured change in conductance and corresponding fit to the HLN equation for $\text{Bi}_2\text{Se}_3\text{-In}_2\text{Se}_3\text{-Bi}_2\text{Se}_3$ with In_2Se_3 thickness of 2 and 50 QL (see Supplemental Materials for more data) (b,c) \tilde{A} extracted from the HLN formula plotted versus thickness of the In_2Se_3 layer in $\text{Bi}_2\text{Se}_3\text{-In}_2\text{Se}_3\text{-Bi}_2\text{Se}_3$ (30- t -30 QL): the curves are an empirical function defined in the text. (b), and $\text{Bi}_2\text{Se}_3\text{-In}_2\text{Se}_3\text{-Bi}_2\text{Se}_3\text{-In}_2\text{Se}_3\text{-Bi}_2\text{Se}_3$ (30-20-30- t -30 QL) (c). (d) Calculations of the energy gap at the interface of $\text{Bi}_2\text{Se}_3\text{-In}_2\text{Se}_3$ at the Γ point showing that the gap at the Dirac point closes as the In_2Se_3 thickness increases. (e-h) Schematic of the heterostructure formed for increasing In_2Se_3 thickness alongside the calculated real space density of the states (RDOS) around the Fermi level as a function of thickness, showing the emergence and decoupling of the interfacial states with thickness.

Figure 3. (Color online) Composition and thickness-dependent coupling parameters extracted from weak-antilocalization effect for $\text{Bi}_2\text{Se}_3\text{-(Bi}_{1-x}\text{In}_x)_2\text{Se}_3\text{-Bi}_2\text{Se}_3$ films. (a) Schematic showing the $\text{Bi}_2\text{Se}_3\text{-(Bi}_{1-x}\text{In}_x)_2\text{Se}_3\text{-Bi}_2\text{Se}_3$ structure where the coupling can be modulated by changing the barrier thickness or height. (b-d) \tilde{A} for $\text{Bi}_2\text{Se}_3\text{-(Bi}_{1-x}\text{In}_x)_2\text{Se}_3\text{-Bi}_2\text{Se}_3$ with fixed composition while varying thickness, and (e-g) with fixed thickness while varying composition. Symbols are experimental data, and the lines are fits to

the empirical function (see text). (h) Compositional dependence of the fitting parameters extracted from the curves in (b-d) and Fig. 2(b). Here t_0 gives the critical thickness for the $\tilde{A} = 1 \rightarrow 2$ transition, while l_0 is the width of the transition region. (i) Contour plot of the empirical function for \tilde{A} as a function of x and t for $x \gtrsim 25\%$; below $x \approx 25\%$, we took \tilde{A} to be 1 due to the metallic nature of the barrier in this regime.

Figure 1 (two-column)

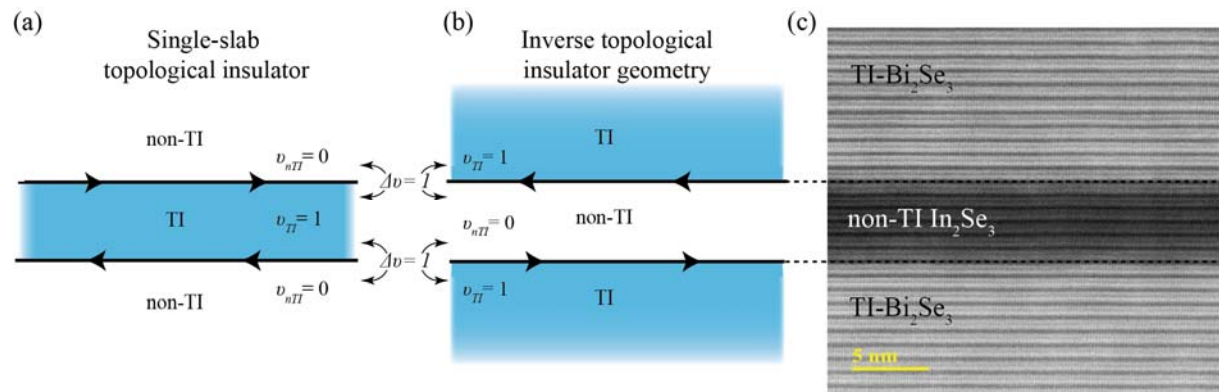


Figure 2 (two-column)

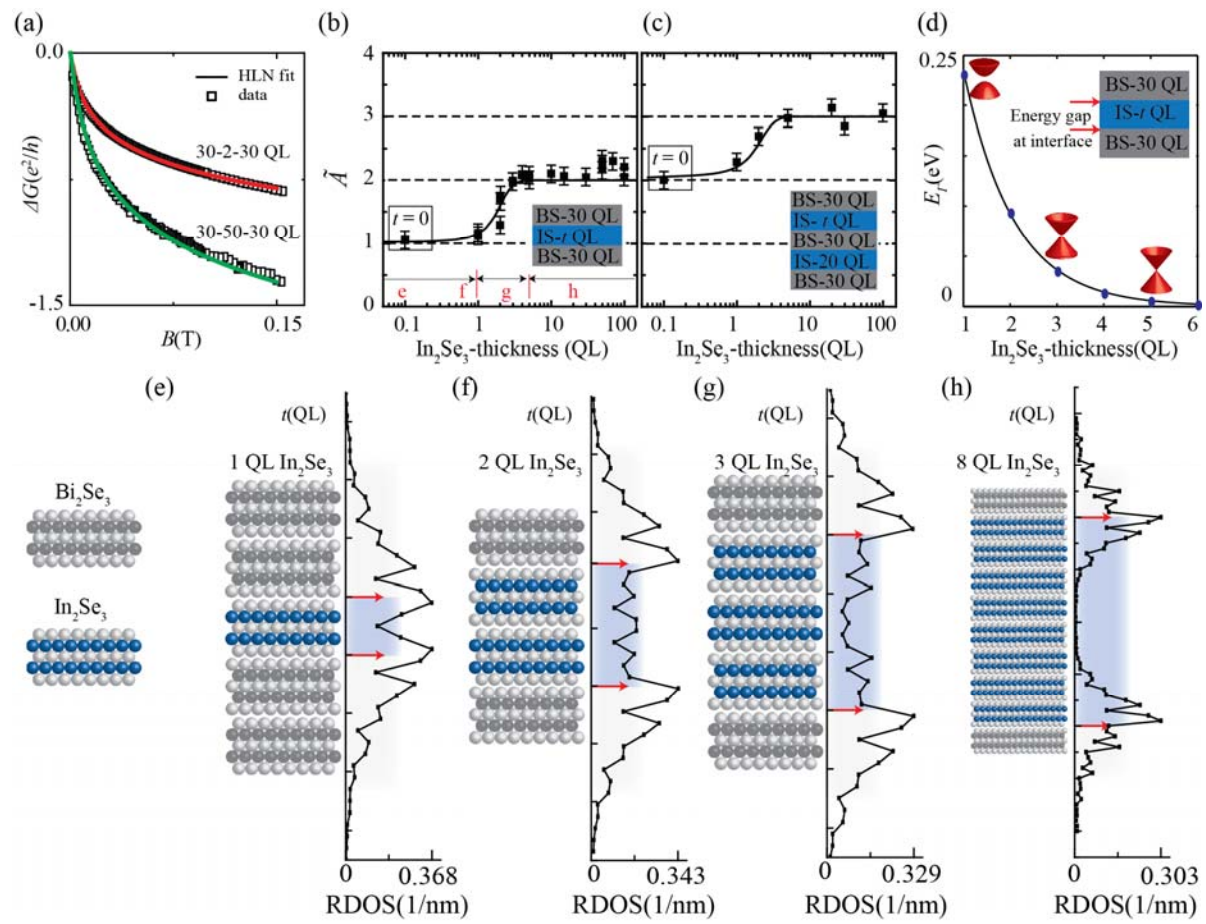


Figure 3 (two-column)

